HHS Public Access

Author manuscript

Phys Med Biol. Author manuscript; available in PMC 2019 January 16.

Published in final edited form as:

Phys Med Biol. ; 63(2): 025030. doi:10.1088/1361-6560/aa9910.

A line fiducial method for geometric calibration of cone-beam CT systems with diverse scan trajectories

M. W. Jacobson[1], **M. D. Ketcha**[1], **S. Capostagno**[1], **A. Martin**[1], **A. Uneri**[1], **J. Goerres**[1], **T. De Silva**[1], **S. Reaungamornrat**[2], **R. Han**[1], **A. Manbachi**[1], **J. W. Stayman**[1], **S. Vogt**[3], **G. Kleinszig**[3], and **J. H. Siewerdsen**[1,2]

[1]Department of Biomedical Engineering, Johns Hopkins University, Baltimore MD, 21205 USA

[2]Department of Computer Science, Johns Hopkins University, Baltimore MD, 21218 USA

[3]Siemens Healthcare XP Division, Erlangen, Germany

Abstract

Modern cone-beam CT systems, especially C-arms, are capable of diverse source-detector orbits. However, geometric calibration of these systems using conventional configurations of spherical fiducials (BBs) may be challenged for novel source-detector orbits and system geometries. In part, this is because the BB configurations are designed with careful forethought regarding the intended orbit so that BB marker projections do not overlap in projection views. Examples include helical arrangements of BBs (Rougee *et al* Proc. SPIE **1897** 161–9) such that markers do not overlap in projections acquired from a circular orbit and circular arrangements of BBs (Cho *et al* Med Phys **32** 968–83). As a more general alternative, this work proposes a calibration method based on an array of line-shaped, radio-opaque wire segments. With this method, geometric parameter estimation is accomplished by relating the 3D line equations representing the wires to the 2D line equations of their projections. The use of line fiducials simplifies many challenges with fiducial recognition and extraction in an orbit-independent manner. For example, their projections can overlap only mildly, for any gantry pose, as long as the wires are mutually non-coplanar in 3D. The method was tested in application to circular and non-circular trajectories in simulation and in real orbits executed using a mobile C-arm prototype for cone-beam CT. Results indicated high calibration accuracy, as measured by forward and backprojection/triangulation error metrics. Triangulation errors on the order of microns and backprojected ray deviations uniformly less than 0.2 mm were observed in both real and simulated orbits. Mean forward projection errors less than 0.1 mm were observed in a comprehensive sweep of different C-arm gantry angulations. Finally, successful integration of the method into a CT imaging chain was demonstrated in head phantom scans.

Keywords

geometric calibration; cone-beam CT; line fiducial; wire phantom; BB phantom; C-arm

Corresponding Author: Jeffrey H. Siewerdsen, PhD, jeff.siewerdsen@jhu.edu, Johns Hopkins University, Traylor Building, Room 622, 720 Rutland Avenue, Baltimore MD 21205.

1 INTRODUCTION

Accurate, high-quality image reconstruction in cone-beam CT (CBCT) benefits from accurate calibration and reproducibility of the system geometry. Circular source-detector orbits represent the most common scan geometry for a broad range of CBCT systems including systems for dental (Pauwels 2015), breast (Boone *et al* 2001, Bian *et al* 2014), and extremity (Carrino *et al* 2014) imaging as well as image-guided radiotherapy (Jaffray *et al* 2002)). However, a considerable area of research involves alternative, non-circular geometries. Interest in non-circular scans is motivated in part by projection data incompleteness inherent in circular CBCT scans. Orbits such as circular sinusoids as well as those composed of multiple arcs, lines, and ellipses (Noo et al. 1998; Katsevich 2004; Katsevich 2005) have been shown to provide more complete object coverage and thereby to eliminate or reduce cone-beam artifacts. Further benefits to non-circular orbits include increased field of view (FOV). Combinations of rotation and gantry translation have been shown, for example, to achieve the same FOV as in C-arm systems, but with reduced gantry size (Ritschl *et al* 2016). A selection of such orbits is illustrated in Figure 1, some of which are also investigated specifically in this paper. The sinusoid-on-sphere orbit in Figure 1(a) is akin to the reduced circular sinusoid of (Xia *et al* 2009), except that sinusoidal out-of-plane motion is implemented via gantry rotations rather than translations. Recent work has also presented methods for optimizing orbit geometries to the anatomy of a specific patient and visualization task (Stayman *et al* 2015, Ouadah *et al* 2017), leading to improved detectability of implants and interventional instruments for a given radiation dose. Such optimization can produce particularly irregular orbit shapes, as illustrated in Figure 1(d) for a cochlear implant visualization task (Ouadah *et al* 2017).

Advances in the motion capabilities of mobile and stationary C-arms have created opportunity for CBCT acquisition with considerable flexibility in the selection of source-detector orbits, making such techniques a likely trend in new imaging protocols. In the work reported below, we therefore consider a wide variety of forms in scan trajectory and propose a flexible and accurate method for geometric calibration of such systems.

Geometric calibration is the process of estimating the system parameters that relate the position of points in the 3D image reconstruction to their projected location in the 2D projection data. For a point x-ray source and area detector, the system geometry is described by 9 degrees of freedom (DOF) describing the location of the source and the location and orientation of the detector for each projection view. In practice, geometric calibration in CBCT is most commonly performed by scanning a known 3D configuration of radio-opaque BB fiducials (Noo *et al* 2000, von Smekal *et al* 2004, Cho *et al* 2005, Yang *et al* 2006, Mennessier *et al* 2009, Li *et al* 2010, Hu *et al* 2011). By relating the observed 2D locations of the BB projections to their known 3D template, an inversion problem can be solved to obtain the parameters.

Calibration methods (including the one described below) that rely on pre-scans of a phantom are classified as *offline* methods and assume that the geometry as computed during calibration remains valid in subsequent scans. This appears to be a reasonable assumption for many systems. In some cases, a less strict assumption is made that the continuous

source-detector trajectory is repeatable from scan to scan, but that the gantry positions along the trajectory may vary slightly due to imperfect synchronization between gantry motion and each projection. In such situations, gantry motor position sensors (e.g., encoders) can be used to determine where along the continuous trajectory the projections were acquired. The gantry poses in the patient scan can then be interpolated from the poses in the calibration scan.

A problem with BB-based methods, however, is that they are not generally applicable to a diversity of orbits, except perhaps by implementing a different marker phantom and calibration software routine for every orbit of interest. This is because the marker phantom and accompanying software are normally designed with respect to a particular anticipated orbit shape (usually circular) to prevent marker projection overlap and to allow a BB projection to be identified appropriately with its 3D model. As an example, in a helical BB configuration (Rougee *et al* 1993), the BBs are spaced longitudinally to ensure that marker projections do not overlap as the system rotates circularly. Longitudinal separation also ensures that a given 2D marker projection can be matched easily to its 3D model based on its axial position in the projection view. As another example, in the 2-ring BB phantom design due to (Cho et al 2005), marker images are distributed around the periphery of an ellipse and, in a circularly rotating system (see Figure 2(a)), always maintain a fixed order reflecting their 3D positions. Such designs, however, do not easily accommodate scan trajectories with longitudinal, out-of-plane gantry motion. This is especially true for C-arm geometries having relatively small area detectors. For such systems, the BBs must be spaced more densely so that they are visible within the projection field of view (FOV).

For such systems, the BBs must be spaced more densely so that they are visible within the projection field of view (FOV). With the tighter spacing comes an increased likelihood of BB projection overlap. For established BB phantoms, overlap may occur even for out-of-plane angulations of the source as small as 5° - for example, in the sinusoidal scan geometry of Figure 1(a), illustrated further in Figure 2(b) with simulated projections of a 2-ring BB phantom.

Possible solutions to these issues include so-called *online* calibration methods that do not use dedicated phantoms (Kyriakou *et al* 2008, Panetta *et al* 2008, Patel *et al* 2009, Wicklein *et al* 2012, Ouadah *et al* 2016). Instead, these methods estimate geometry directly from the patient scan. Online methods are generally intended to address cases in which the acquisition geometry is imperfectly reproducible from scan to scan, e.g., due to unrepeatable gantry motion or patient motion. When reproducibility is not a concern, these methods can also be used to pre-calibrate the system in a traditional offline manner. Some methods within this category employ data redundancy conditions (Panetta *et al* 2008, Patel *et al* 2009) that only hold true for certain orbit geometries. Other online methods enforce anticipated properties in the 3D image reconstruction via iterative optimization (Kyriakou *et al* 2008, Wicklein *et al* 2012). The latter methods are more generally applicable to diverse orbit geometries, as are methods based on 3D-2D registration (Ouadah *et al* 2016, Berger *et al* 2016). However, because they involve iterative forward and back projection operation, their flexibility comes with considerable computational expense.

The solution proposed in this work is a phantom-based method for geometric calibration that, instead of BBs, uses an array of line-shaped fiducials formed from segments of radio-opaque wire. Geometric parameter estimation is accomplished by relating the 3D line equations representing the wires to the 2D line equations of their projections. While line-shaped features have long been used for calibration of photographic cameras (Cipolla *et al* 1999, Caprile and Torre 1990, Liebowitz and Zisserman 1999), line fiducial methods have not been applied in CBCT calibration, to our knowledge. An 8-wire phantom (Figure 3) is proposed as an initial design and tested in application to circular and non-circular C-arm motion.

The use of line fiducials is more generally adaptable to a diversity of non-circular orbits than traditional BB methods in at least 3 respects. First, 2D projections of 3D lines can intersect at no more than a single point, for any gantry pose, as long as the 3D lines are mutually non-coplanar. Since 2D line segment detection is not confounded by a single point of intersection, problems of fiducial overlap are avoided in a highly orbit-independent way. For technical reasons to be discussed below, the design in Figure 3 does include some coplanar wires, but by keeping these sufficiently spaced apart, the phantom is able to accommodate a significant range of circular and non-circular orbits. Second, because each wire projection is identified by two line segment endpoints, they lie far apart in a 4D feature space (see Section 2.2) and can be robustly tracked from view-to-view for fiducial identification purposes. This is in contrast to BB projection tracking, which may be confounded if two BB projections overlap or lie in close proximity. When this occurs, the BBs may be mis-identified in all subsequent views unless specific knowledge of the orbit geometry is used to resolve the ambiguity. Third, line-based calibration is less adversely affected if the phantom is not completely contained in the viewable region of the x-ray detector, a scenario that is likely to occur for at least some gantry positions in complicated orbit geometries. In such gantry positions, a BB near the edge of the phantom may be completely unviewable, and any information about the view geometry encoded in that particular BB is lost. Conversely, line fiducial phantoms can be designed so that all line markers extend deep into the center of the field of view, making them more robustly visible. Note that only a section of a line fiducial (not its whole length) need be visible for its 2D line equation to be determined and for constraining information on the projection geometry (equation (3) in Section 2) to be obtained.

In the following sections, details of the calibration method are presented, including phantom design, fiducial extraction, and parameter estimation. Calibration performance was quantified in terms of forward projection accuracy metrics, backprojection/triangulation accuracy metrics, and with respect to accuracy in estimating source-detector pose parameters. The method was further tested in application to circular and non-circular phantom scans, both in simulation and using real data acquired on a prototype mobile C-arm. Performance comparisons between wire-based and BB-based calibrations of circular orbits are also presented with respect to point spread function (PSF) width and visualization of fine features in trabecular bone in a head phantom.

2 METHODS

2.1 A Parametric Model for Line Projections

In this section, we derive a parametric model for the projections of 3D lines that will serve as a basis for the wire-based geometric calibration method. We write the parametric equation for a 3D line in homogeneous coordinates as

$$\boldsymbol{L}(t)=\boldsymbol{X}+t\boldsymbol{D}.$$

where $\boldsymbol{X} = [X^T, 1]^T$ and $\boldsymbol{D} = [D^T, 0]^T$ are 4×1 homogeneous vectors representing, respectively, a point on the line and the line's direction. The 3×1 vectors X and D denote the same in inhomogeneous coordinates. As a general convention throughout the paper, vectors in **bold type** will denote homogeneous coordinate vectors to distinguish them from inhomogeneous coordinate vectors.

The geometry of a flat panel detector cone-beam CT system in a particular gantry position can be specified by nine parameters. In the parametrization considered here (see Figure 4(b)), three of the nine parameters are the position coordinates of the x-ray source, expressed as the vector $C = [c_x, c_y, c_z)^T$. Three additional parameters are the Euler angles defining detector orientation expressed as the vector $\theta = [\theta_1, \theta_2, \theta_3)^T$. The final three are the so-called intrinsic parameters consisting of the Source-Detector Distance (SDD) and the 2D piercing point coordinates (u_0, v_0) where C projects orthogonally to the detector. We let $\alpha = [\mathrm{SDD}, u_0, v_0)^T$ denote the vector of intrinsic parameters collectively. A 3D homogeneous coordinate $\boldsymbol{X}$ and the 2D homogeneous point $\boldsymbol{x}$ to which it projects are related according to $\boldsymbol{x} = P\boldsymbol{X}$, where P is a 3×4 projection matrix of the form,

$$P=K_\alpha R_\theta[\ I\ \ -\mathrm{C}\ ], \quad (1)$$

$$K_\alpha=\begin{bmatrix} \mathrm{SDD} & 0 & u_0 \\ 0 & \mathrm{SDD} & v_0 \\ 0 & 0 & 1 \end{bmatrix} \quad (2)$$

Here, $R_\theta = [R_{\theta,u}\, R_{\theta,v}\, R_{\theta,w}]^T$ is a 3×3 rotation matrix, parameterized by the angles θ. The columns $R_{\theta,u}$, $R_{\theta,v}$ and $R_{\theta,w}$ of the matrix R_θ^T are the directions of the detector axes.

Under cone-beam projection, a 3D line $\boldsymbol{L}(t)$ maps to a 2D line whose equation $\mathrm{a}_i u + \mathrm{b}_i v + \mathrm{c}_i = 0$ is compactly expressed as $\boldsymbol{l}^T\boldsymbol{x} = 0$. Here $\boldsymbol{x} = [u, v, 1]^T$ is a homogeneous point on the line and $\boldsymbol{l} = [\mathrm{a}_i, \mathrm{b}_i, \mathrm{c}_i]^T$ is a homogeneous vector of equation coefficients. Because the projections of all points on the 3D line satisfy the 2D line equation, we have $\boldsymbol{l}^T P\boldsymbol{L}(t) = 0$ for all t. Considering this relation at $t = 0$ directly yields $\boldsymbol{l}^T P\boldsymbol{X} = 0$. Considering $t = -1$ leads further to $\boldsymbol{l}^T P\boldsymbol{D} = \boldsymbol{l}^T P\boldsymbol{X} = 0$. These observations can be combined to give,

$$\boldsymbol{l}^T P[\boldsymbol{X}, \boldsymbol{D}]=0. \quad (3)$$

By incorporating the above decomposition into (3), we obtain

$$\boldsymbol{l}^T K_\alpha R_\theta X=\boldsymbol{l}^T K_\alpha R_\theta C, \quad (4)$$

$$\boldsymbol{l}^T K_\alpha R_\theta D=0 \quad (5)$$

An alternative statement of (3) is that the equation vector $\boldsymbol{l}$ is orthogonal to both $P\boldsymbol{X}$ and $P\boldsymbol{D}$ and therefore can be obtained from their cross-product $\boldsymbol{l} = P\boldsymbol{X} \times P\boldsymbol{D}$. Incorporating (1) into the cross-product[1] leads to the following explicit solution for $\boldsymbol{l}$:

$$\boldsymbol{l}=K_\alpha^{-T} R_\theta (X \times D - C \times D). \quad (6)$$

It is a well-known result (Hartley and Zisserman 2003, p. 214) that parallel 3D lines do not generally project to parallel 2D lines, but rather to lines intersecting at a so-called vanishing point $\boldsymbol{v} = K_\alpha R_\theta D$. Here, D is the common direction of the parallel 3D lines. Equation (5) shows that $\boldsymbol{v}$ lies on the projection $\boldsymbol{l}$ of any 3D line with direction D, and is therefore consistent with this result. The exception is when D is parallel to the plane of the x-ray detector, in which case the imaged lines will also be parallel. Although equation (5) is still satisfied in this case, the vanishing point is a degenerate, non-physical point with homogeneous coordinates $\boldsymbol{v} = [v_1, v_2, 0]^T$.

Equation (3) is analogous to the more traditional relationship,

$$\boldsymbol{x} \times P\boldsymbol{X}=0, \quad (7)$$

which arises in conventional pointmarker based calibration. Here, $\boldsymbol{x}$ is the projected 2D location of any 3D point marker $\boldsymbol{X}$. Similar to (3), two constraints on the projection matrix P arise from (7). Although (7) is a matrix equation composed of three scalar equations, it is known (Hartley and Zisserman 2003, p. 179) that only two of these three are linearly independent.

[1]Here, we make use of the cross-product identity $(Ma) \times (Mb) = \det(M) M^{-T} (a \times b)$, where M is any non-singular matrix. The factor of $\det(M)$ is an irrelevant scaling in this context, however, and has been dropped from equation (6). This is because $\boldsymbol{l}$ is a homogeneous quantity, i.e., a line is unchanged when its equation coefficients are scaled.

2.2 Geometric Calibration Method

The proposed geometric calibration method begins with a scan of the wire phantom to obtain log-scaled projection views in a particular scan geometry. The projection data are then processed in a chain of 3 main stages shown in Figure 4(a) and discussed in the following sub-sections.

Wire Projection Sampling: In this stage, a search is made in each projection view for integer pixel coordinates approximately traversing the projected center-lines of the wires. Because projection rays passing through a wire's center-line have longer attenuation path lengths than off-centered rays, these pixels can be identified (see Figure 4(c)) from local maxima in row-wise and column-wise sweeps through the log-scaled image. An intensity threshold derived from Otsu's method is used to identify the pixel regions occupied by the wire projections and to restrict the search to those regions.

Once a pool of center-line pixels have been collected, an approach based on the Random Sample Consensus Algorithm (RANSAC) due to (Fischler and Bolles 1981) is then used to group the pixels, associating them with different wires. In this process, pixel pairs A and B are randomly drawn from the set S of ungrouped pixels. For each pair of pixels drawn, a search is made in S for further pixels (a so-called consensus set) that lie along a common wire projection containing A and B. Initial candidates for the consensus set are obtained (see Figure 4(d)) from pixels sufficiently colinear with A and B, as tested using a distance tolerance of $2\sqrt{2}$ pixels from the infinite line passing through A and B. A subsequent search, restricted to the tolerance region, is made to reject samples not lying on a common wire with A and B. New pixel pairs are drawn until a sufficiently large consensus set is found, as determined from a preset threshold. When this occurs, it is concluded that a wire has been identified. The pixels for that wire are then removed from the search pool S and the process continues until all wires have been assigned samples. Throughout this work, pixel pitch was in the range 0.3–0.4 mm (2×2 binning of the flat-panel detector described below) and a consensus set threshold of 100 pixels was found to work well for these cases.

3D-2D Matching: Once all pixels lying along a common wire projection have been grouped together, each such group is matched to a particular wire in 3D. To this end, the pixel groups are first used to fit a line segment to each wire projection in each view. This results in the parameterization of each wire projection by a 4-dimensional vector $Q_{AB} = [\, u_A, v_A, u_B, v_B]^T$ where $A = (u_A, v_A)$ and $B = (u_B, v_B)$ are the endpoints of a particular line segment. Note that if the phantom is designed so that the wires form mutually non-coplanar lines in 3D, then their line segment projections can intersect at no more than one point, and therefore their representations Q_{AB} will be very well separated in 4D. The separation between two line segments Q_{AB} and Q_{CD} is quantified as,

$$d(Q_{AB}, Q_{CD}) = \min(\|Q_{AB} - Q_{CD}\|, \|Q_{AB} - Q_{DC}\|),$$

Using this distance measure, wire projections in adjacent views are compared for proximity and tracked from view to view. This leads to a consistent labelling of each wire's projection across views.

Once view-to-view labelling is established, the wire identification problem reduces to matching each wire projection in a single reference view (e.g., the first view acquired) to its 3D model. By positioning the wire phantom so that, in every scan, it faces the detector in approximately the same pose in the reference view, the wire projections will form predictable patterns of slope, elevation, and intersection in that view. A basic pattern recognition routine customized to the phantom (but not to the source trajectory) can therefore be used to complete the 3D-2D matching. As an example, the image of wire $\mathbf{A}'$ in Figure 3(b) is always identifiable - assuming very modest repeatability in phantom positioning - as the unique wire image in the lower half of the projection view which is downward sloping. Similarly, the intersection points of each wire with the image boundary in Figure 3(b) will always have the same clock-wise ordering. These two features are sufficient to uniquely identify all of the wires. An alternative way to accomplish 3D-2D matching, if an approximate nominal geometry estimate is available, is by direct 3D reconstruction of the wires.

Geometry Estimation: The final stage of the calibration pipeline is to estimate, for each view, the geometry parameters α, θ and C from the set of line coordinate samples $\{\boldsymbol{x}_{ij}\}$ collected previously. Here, $\boldsymbol{x}_{ij}$ is a 3×1 homogeneous vector denoting the j-th pixel coordinate sampled from the i-th wire projection in the given view. It is assumed that the wire phantom geometry is known (either from precise design / manufacture or from measurement) with negligible error. In this context, this means that equations for the 3D line $\boldsymbol{L}_i(t) = \boldsymbol{X}_i + t\boldsymbol{D}_i$ passing through each wire, i, are accurately known *a priori* in some coordinate system. Section 2.3.2 describes how the related wire pose data X_i, D_i can be pre-estimated.

As a first step in the process, the input data X_i, D_i, $\boldsymbol{x}_{ij}$, are pre-normalized. The normalization procedure is an adaptation of standard data conditioning methods from conventional point marker-based calibration. We defer the details to the Appendix. Parameter estimates are then obtained by minimizing the least squares cost function,

$$f(\alpha,\theta,C)=\sum_{ij}\left|\boldsymbol{x}_{ij}^{T}K_{\alpha}^{-T}R_{\theta}(X_i\times D_i-C\times D_i)\right|^2. \quad (8)$$

The nonlinear least squares residuals are zero, due to (6), when the samples $\boldsymbol{x}_{ij}$ lie precisely on the modelled lines $\boldsymbol{l}_i=K_{\alpha}^{-T}R_{\theta}(X_i\times D_i-C\times D_i)$. The minimization of f may be accomplished using the Levenberg-Marquardt algorithm, implemented in this work using MATLAB's `lsqnonlin` command. Note that, unlike BB-based calibration, the above estimation procedure does not use 3D-2D point correspondences. The cost function (8) evaluates a geometry estimate based exclusively on algebraic error, i.e., on how well the wire image pixels $\boldsymbol{x}_{ij}$ satisfy 2D line equations arising from that estimate.

Because it is unclear whether f has local minima, the initializing parameter estimates for the iterative minimization cannot be selected arbitrarily. We propose a two-step analytic algorithm for deriving reasonably accurate initial estimates from line fits $\hat{\boldsymbol{l}}_i$ to the samples $\boldsymbol{x}_{ij}$. The steps are as follows:

1. Using (3), a system of linear homogeneous equations in the elements of P is obtained, with two equations $\hat{\boldsymbol{l}}_i^T P[\boldsymbol{X}_i, \boldsymbol{D}_i]=0$ contributed by each wire. The total system of equations is solved algebraically to give an initial estimate $\hat{P}$ of the projection matrix. Similar to equation (1), the estimate has a decomposition $\hat{P}=K\hat{R}_\theta[I-C]$, except that, because the algebraic solution is unconstrained, K will be a general upper-triangular matrix, rather than one with the specific form (2). The decomposition of $\hat{P}$ is made using the QR-algorithm, resulting in an estimate $\hat{R}_\theta$ of the detector orientation.

2. Using (4) and (5), and the estimate $\hat{R}_\theta$ obtained in the previous step, we construct the equations,

$$\hat{\boldsymbol{l}}_i^T K_\alpha \hat{R}_\theta X_i=\hat{\boldsymbol{l}}_i^T q, \quad (9)$$

$$\hat{\boldsymbol{l}}_i^T K_\alpha \hat{R}_\theta D_i=0 \quad (10)$$

where we have made the change of variables $q=K_\alpha\hat{R}_\theta C$. Here again, each wire contributes 2 equations. These equations form a linear system in α and q which are solved to obtain estimates of α and $C=(K_\alpha\hat{R}_\theta)^{-1}q$.

Because this initialization technique involves almost purely algebraic operations, it has the advantages of both speed and flexibility. No specific assumptions about the wire configuration or scan geometry are used, other than that the various equations involved possess well-defined solutions. This will depend on the chosen 3D configuration of wires, as discussed in the next section.

With the geometry estimation procedure above, a solution is obtained with respect to the pre-normalized X_i, D_i, $\boldsymbol{x}_{ij}$ data. As a final step, the corresponding estimated projection matrix $\hat{P}$ can be mapped back to the original coordinate system as described in the Appendix.

2.3 Multi-Wire Calibration Phantom Design

2.3.1 Nominal Phantom Design—As mentioned earlier, an advantageous design choice for a multi-wire calibration phantom is to have the wire segments be mutually non-coplanar, as this avoids fiducial projection overlap in all gantry poses. However, the wire configuration must also be selected so that the geometry estimation is a well-posed inverse problem. While necessary and sufficient conditions are known (Buchanan 1988) for an array of point markers to uniquely determine the geometry, a comparable characterization for line-shaped

markers has not been previously reported, to the best of our knowledge. Sufficient conditions for invertibility can be deduced, however, from the known theory of vanishing points. This motivated a nominal 8-wire phantom design, as discussed below. The nominal design is depicted in Figure 3(a). Parametric line equation data for the 8 wires are listed in Table 1. A compromise made in this design is the inclusion of parallel, and therefore coplanar, wire pairs. Nevertheless, by spacing the parallel wires sufficiently far apart, fiducial overlap is avoided while still allowing the phantom to accommodate a broad range of circular and non-circular scan trajectories.

The computer vision literature has established (Cipolla *et al* 1999, Caprile and Torre 1990, Liebowitz and Zisserman 1999) that if a triad of non-degenerate vanishing points $\boldsymbol{v}_i = K_a R_\theta D_i$, $i = 1, 2, 3$ from orthogonal directions D_i can be identified in a projection image, then these points can be used to calculate the view geometry. Based on this result, we have designed the phantom to contain an orthogonal, mutually non-coplanar set of wires labelled **A**, **B**, and **C** in Figure 3 with parallel counter-parts **A′**, **B′**, and **C′**. A gap of 3 cm separates the wire pairs longitudinally so that parallel wires cannot have overlapping projections except for large out-of-plane gantry angulations (about 40° for typical C-arm geometries). The presence of these parallel pairs ensures that 3 vanishing points can be determined from the intersection of their images. This being said, in the interest of incorporating both orthogonally and non-orthogonally oriented wires into the computation, the geometry estimation method of Section 2.2 does not use established vanishing point methods. However, the *option* of resorting to vanishing point methods guarantees invertibility, except at gantry poses for which the detector is parallel to one or more of these wires. In such cases, the corresponding vanishing points will be degenerate and the invertibility of the estimation problem is uncertain.

Because the availability of 3 non-degenerate vanishing points is merely a sufficient condition, it is not clear whether their absence is genuinely a problem. If it is a problem, it is possible that data from additional wires, non-orthogonally oriented with respect to the triad **A**-**A′**, **B**-**B′**, **C**-**C′**, might compensate for information lost when a degenerate view of the triad is reached. With this in mind, we have included an additional pair of parallel wires **D**-**D′** oriented at 45° to **B**-**B′** and **C**-**C′**. This choice was based simply on intuition and experimentation; however, in tests of the phantom in Section 3, we observed negligibly small calibration errors, even at views where degeneracy occurred.

2.3.2 Prototype Phantom Implementation and Wire Pose Determination—The proposed calibration method assumes that for each fixed wire, i, line parameters X_i, D_i describing the 3D pose of the wire be known *a priori* with negligible error. This is analogous to traditional BB-based calibration which supposes a known 3D model for the BB locations (although extensions may be possible, similar to (Xu *et al* 2017)). With sophisticated manufacturing resources, it may be possible to precisely fabricate the wire phantom so that desired X_i, D_i are achieved with high accuracy. An alternative approach is to construct the phantom with approximately desired dimensions and then obtain more precise estimates of X_i, D_i from standard circular CBCT scans of the phantom on a well calibrated system. In this work, for the sake of cost and prototyping flexibility, we followed the latter course. The prototype wire phantom, composed of foam blocks and 3D-printed wire mounts, is shown in

Figure 3(b). The wires were manually placed to mimic the nominal pose data in Table 1. Estimates of the actual wire pose parameters X_i, D_i were derived from a scan with the CBCT system shown in Figure 5(d).

An intuitive way to determine the wire poses from a calibrated CT scan is to segment the wires from a 3D CT reconstruction and fit 3D lines to the wire voxels directly. We chose an alternative that works instead with line fits $\hat{\boldsymbol{l}}_i$ to samples $\boldsymbol{x}_{ij}$ extracted from the acquired projection images. This leads, as before, to equations (9) and (10), except that in this case, because the CT scan geometry is pre-calibrated, the unknowns in the equations are the wire pose parameters X_i and D_i. For each fixed i, two independent linear equations are contributed by each projection view. Solving these linear equations leads to estimates of the wire poses.

Because the 3D parametrization of a line is non-unique, there is a 1D space of solutions X_i to (9). Since the geometry estimation cost function in equation (8) depends on X_i entirely through $X_i \times D_i$, any point X_i on the line may in theory be selected without affecting the calibration process. For numerical conditioning reasons, however, we recommend that the chosen X_i not vary greatly in magnitude from wire to wire. In our work, we chose an X_i from the solution space lying approximately at the inner-most wire tips (i.e., the tips closest to the center of the phantom). This was largely a matter of preference, however, and was not intended to accurately represent the wire tip locations.

Applying the above procedure to the phantom in Figure 3(b) led to the pose estimates listed in the lower half of Table 1. There are noticeable discrepancies between the nominal and implemented wire poses due to errors in manual placement. Also, because the implemented triad **A-A′, B-B′, C-C′** is not ideally orthogonal, it is natural to ask whether the arguments for the design in Section 2.3.1 are still valid. However, the effectiveness of the phantom and the pose estimates in Table 1 are confirmed by experiment in Section 3.

2.4 Experimental Methods

Experiment #1A: Simulation Tests of Geometry Estimation Accuracy: In a first set of simulation tests, we examined the extent to which the 8-wire configuration provided accurate estimates of various gantry poses. Synthetic line projection samples $\boldsymbol{x}_{ij}$ of our prototype wire phantom implementation (with pose data X_i, D_i from the lower part of Table 1, not the nominal design) were generated for a hypothetical isocentric C-arm geometry with a 40 cm × 40 cm detector area and .308 mm pixel pitch. In the ground truth geometry, the SDD was 120 cm and the Source-Isocenter Distance (SID) was 78.5 cm. Data were generated (see Figure 5(a)), for a range of gantry angulations uniformly sampled in spherical coordinates. The sampling was at 2° increments with respect to both in-plane azimuthal gantry positions, $0° \le \varphi \le 360°$, and out-of-plane gantry elevations, $-40° \le \psi \le 40°$. The range of gantry elevations considered here is consistent with anti-collision constraints in typical scan scenarios. Out-of-plane elevations greater than 40° would normally risk gantry collision with the patient or table.

The samples $\boldsymbol{x}_{ij}$ were generated from noise-free, analytic projections of the wires under the known ground truth geometry. To these, 50 realizations of Gaussian errors were then added

so as to displace them perpendicularly from the true *i*-th wire location. The number of samples along the length of each wire projection was selected as max (*H*, *W*), where *H* and *W* are the height and width of the wire projection in pixels. The variance of the Gaussian noise was chosen to produce root mean squared (RMS) perpendicular deviations from the true line of 0.093 mm (or 0.30 pixels). This choice was in agreement with RMS line fit residuals observed in actual wire phantom scans (at 70 kV, 100 mAs) taken on the mobile C-arm (Figure 5(d)). Geometry estimates were then derived from each of the 50 realizations. The tests here focused exclusively on the geometry estimation step and not the full processing chain of Figure 4(a). It is for this reason that the samples $\boldsymbol{x}_{ij}$ were generated directly and not from simulated x-ray images.

The accuracies of the geometry estimates were first assessed in terms of magnification-corrected reprojection error (RPE), a forward projection accuracy metric:

$$\text{Mag. Corrected RPE} = \frac{d(\hat{P}\boldsymbol{X}, P\boldsymbol{X})}{\text{SDD}/\text{depth}(\boldsymbol{X})}$$

Here, $d(\hat{P}\boldsymbol{X}, P\boldsymbol{X})$ is the Euclidean distance between the ideal forward projection $P\boldsymbol{X}$ of a 3D test point $\boldsymbol{X}$ and its estimated projection $\hat{P}\boldsymbol{X}$. This is normalized by SDD/depth($\boldsymbol{X}$), the usual cone beam magnification at $\boldsymbol{X}$. This was evaluated, for all 50 realizations and gantry positions, for a set of 16 test points distributed over a 13 × 13 × 11 cm^3 region of the FOV.

In further simulations of the same gantry geometry, synthetic $\boldsymbol{x}_{ij}$ were generated for the three scan orbits (circular short scan, sinusoid-on-sphere, and task-driven) shown in Figure 1(a) and (d). The circular and sinusoidal orbits consisted of a 200°/498 view arc in-plane. The sinusoid-on-sphere trajectory was then derived by adding a sinusoidally-varying series of out-of-plane gantry tilts to the circular trajectory with a 5° amplitude. This amplitude was sufficient to produce a 14 cm peak-to-peak longitudinal variation in the x-ray source position. The task-driven orbit consisted of 336 views.

Repeated calibrations of these orbits were then performed, again for 50 realizations of $\boldsymbol{x}_{ij}$ with 0.30 pixel simulated errors. The orbit calibrations were then assessed quantitatively in terms of two forms of backprojection error metric – the ray deviation, *d*, and triangulation error, Δ. The same set of 16 test points were forward projected using ground truth geometric knowledge of the orbits. The 50 geometry estimates were then used to triangulate the locations of the 16 points from their projected coordinates, as illustrated in Figure 5(b). The triangulated position of the *m*-th test point X_m^* was obtained as the linear least squares solution to,

$$X_m^* = \text{argmin}_X \sum_k d^2(X, r_{km}).$$

where $d(\cdot, r_{km})$ is the Euclidean distance to r_{km}, the back-projected ray from the *m*-th test point projection in the *k*-th view. The triangulation error was then computed as

$$\Delta \equiv \|X_m^* - X_m\|$$

where X_m is the ground truth location of the m-th marker. The ray deviations were computed as $d(X_m^*, r_{km})$. In other words, they measure the spread of the rays around the triangulated point, and hence the degree of distortion likely to propagate into CT image reconstruction from backprojection error.

Lastly, for the same 3 orbits above and the various noise realizations mentioned, we computed errors in the source position, the pose of the detector panel, and the magnification SDD/depth($\boldsymbol{X}$) at the 16 test points.

Experiment #1B: Simulated Integration into a CBCT Imaging Chain: In a second simulation study, the full calibration pipeline of Figure 4(a) was applied to the imaging of a digital head phantom. The phantom (Figure 5(c)) contained 2 stacks of high contrast disks of alternating intensity (830 HU and −170 HU). Synthetic projection views with pixel pitch 0.616 mm were generated for the digital head in both the circular and sinusoidal orbits of Figure 1(a) using a trilinear interpolating forward projector. Projections of the 8-wire calibration phantom with pixel pitch 0.308 mm phantom were simulated in the sinusoidal orbit using analytic line integrals. No projection noise was added, since the phenomena of interest in this particular experiment were exclusively geometric.

The multi-wire calibration procedure was used to compute the sinusoidal geometry, and the head was then reconstructed from the sinusoidal orbit projections with the Penalized Weighted Least Squares (PWLS) model-based algorithm. Axial resolution was quantified by fitting Gaussian error functions

$$\mathrm{ESF}(z) = a + \frac{b}{2}\left(1 + \mathrm{erf}\left(\frac{z - z_0}{\sigma\sqrt{2}}\right)\right)$$

to the edge spread function (ESF) of the flat disk boundaries, with the σ parameter serving as a measure of ESF width. The same procedure was applied to the simulated circular orbit, except that the ground truth geometry was used in the PWLS reconstruction. Both reconstructions used a voxel size of 0.6 mm. Regularizing penalty weights were chosen to approximately match ESF width to σ=0.1 mm at the disk edge nearest the central axial plane (see Figure 7(c)) for the circular and sinusoidal reconstructions. PWLS cost function minimizations were implemented with 20 iterations of the OS-MOM2 algorithm (Kim *et al* 2015) with 10 ordered subsets. To facilitate comparison, both iterative reconstructions were initialized with the same volume, reconstructed from the circular orbit using the Feldkamp-Davis-Kress (FDK) algorithm (Feldkamp *et al* 1984). In realistic sinusoidal scans, an initial reconstruction would be obtained from an analytic reconstruction algorithm appropriate to the sinusoidal orbit shape, e.g., (Xia *et al* 2009).

Experiment #2: Comparison with BB-based Calibration in a Real Circular Scan Orbit: The proposed wire-based calibration method was compared to conventional BB-

based calibration in real circular scans performed using the prototype C-arm shown in Figure 5(d). The system has an SDD of approximately 110 cm, an SID of 65 cm, and a 30 cm × 30 cm detector area. Geometric calibrations of this system were performed with both the 8-wire phantom and the 2-ring BB phantom (Cho *et al* 2005). Like the simulated version in Figure 2(a), the BB-phantom was of diameter 10 cm with 8 BBs in each ring and a ring separation of 9 cm. For the BB-based calibrations, parameter estimates were obtained using a standard iterative least squares approach using the Levenberg-Marquardt algorithm (Hartley and Zisserman 2003).

Three data sets were acquired. The first was a scan of a triangulation target phantom, consisting of 4 spherical lead markers mounted on a flat foam surface. The triangulation markers were spread over a 12 cm lateral by 12 cm longitudinal area of the 16 cm × 16 cm × 14 cm field of view (FOV). Centroid locations were calculated for each marker in each acquired view and used to triangulate the 4 markers. Triangulation ray deviations were thus computed for both calibration methods. The difference between the triangulated marker locations, as determined from the wire-based and BB-based calibrations, was also calculated.

Next, a phantom containing several slanted wires (0.1 mm diameter steel - not the 8-wire calibration phantom) was scanned for the purpose of calculating point spread function (PSF). FDK reconstructions using both calibrations were made of the phantom with 90% Hamming filter cut-off frequency and voxel size 0.3 mm. Gaussian PSF fits were then derived from samples taken from 45 sub-volumes, each approximately 1 cm^3 and centered around different sections of slanted wire. Finally, a head phantom with natural temporal bone detail was imaged (93 kV, 120 mAs, 350°/560 views). FDK reconstructions using both calibrations were performed, again with 90% Hamming filter cut-off frequency and voxel size 0.3 mm.

Experiment #3: Application to a Three-Arc Orbit on a Mobile C-arm: The wire-based calibration method was tested on a real, non-circular trajectory implemented on the mobile C-arm CT prototype. The C-arm was equipped with an external motion controller capable of driving the arm in pre-programmed sequences of propeller and orbital rotations. The nominal orbit, illustrated in Figure 1(b) was a 3-arc sequence consisting of a 200° propeller rotation (equivalent to 180° + fan angle), followed by a 6° orbital/longitudinal rotation, and finally a 160° propeller rotation with the gantry remaining at a 6° orbital tilt. The increased axial coverage of this orbit gives similar benefits relative to a circular scan as seen for the sinusoidal orbit in Experiment #1B. A convenience of this choice of scan geometry is that an FDK initializer for iterative reconstruction can be readily derived from the 200° arc.

The head phantom shown in Figure 5(e) was scanned in this orbit at 90 kV, 170 mAs. A circular scan at 90 kV, 120 mAs was also acquired. Similar to Experiment #1B, the phantom contained two stacks of high contrast polyethylene and Teflon disks. The head phantom was centered longitudinally on the plane of the circular scan and on the plane of the initial 200° section of the 3-arc scan. Quadratically Penalized Poisson Likelihood (PPL) reconstructions were made from both scans with cost function minimizations implemented with 20 iterations of the OS-SQS algorithm (Erdoğan and Fessler 1999) with 10 ordered subsets. The circular

scan was reconstructed using a BB-based calibration to imitate a conventional CT imaging chain, while the 3-arc scan used wire-based calibration. Both iterative reconstructions were initialized with an FDK image derived from an initial 180° + fan arc. ESF fits to the disk edges were also made as in Experiment #1B and were used to verify approximate resolution matching in the two reconstructions at the disk edge nearest to the central axial plane of the head phantom.

3 RESULTS

Experiment #1A: Simulation Tests of Geometry Estimation Accuracy: Results of Experiment #1A are summarized in Figure 6. The worst-case RPE distributions had median values consistently less than 0.1 mm at all gantry elevations, and an overall maximum error (0.37 mm) that is considerably less than the voxel size (~0.5 mm) typical for C-arm cone-beam CT. The wire-based calibrations showed similarly high back projection accuracy for the 3 orbit geometries considered. Triangulation error was consistently less than 0.012 mm for all noise realizations and markers. Similarly, the ray deviation exhibited a median value of ~0.01 mm for all orbits and was consistently below 0.2 mm for all realizations, markers, and projection views.

Finally, the errors in magnification and source-detector pose are reported for the three orbits in Table 2. For present purposes, the source coordinates $C = [c_u, c_v, c_w]^T$ and the location of the detector center $FP = [FP_u, FP_v, FP_w]^T$ are expressed with respect to rotated axes that align (see Figure 4(b)) with the ground truth detector axes $[R_{\theta,u}\, R_{\theta,v}\, R_{\theta,w}]^T$. In this coordinate system, one can more easily see how depth-related pose parameters (c_w and FP_w) are an order of magnitude more error-sensitive than other parameters. This higher sensitivity is familiar from previous work (Slagowski *et al* 2017, Cho *et al* 2005) on single-view CT calibration. Errors in detector orientation have been quantified in terms of two metrics: angular discrepancy between the ground truth and estimated detector axis $R_{\theta,w}$, which indicates the orientation of the central ray; and the error in panel skew, i.e., the orientation angle within the detector plane of the pixel rows/columns. The latter is known to have more significant impact on image reconstruction (Noo *et al* 1998, Panetta *et al* 2008) than other detector orientation parameters. Error performance reported in Table 2 is similar to, and in some cases exceeds, previously reported results for BB-based methods. In particular, source location, detector location, and skew all show an order of magnitude less error for circular orbits than was reported in (Cho *et al* 2005).

On the whole, these results support the basic feasibility of the wire calibration method, showing it to be robust to realistic levels of noise in the projection data over a wide range of gantry poses. Note also that the calibration remained accurate even at views that should have had degenerate vanishing points in an ideal implementation of the wire phantom. In the circular orbit, for example, the detector plane undergoes a rotation greater than 180° and therefore becomes parallel to each wire segment at some point during the rotation.

Experiment #1B: Simulated Integration into a CBCT Imaging Chain: The image reconstructions for the digital head phantom are shown in Figure 7. In Figure 7(a), cone-

beam artifacts associated with the incomplete geometry of the circular scan are evident as blur (in the *z* direction) for each disk, particularly at increased distance from the central axial plane. Conversely, in Figure 7(b), the sinusoid-on-sphere orbit yields an image reconstruction with sharp edge resolution and an absence of cone-beam artifacts, as expected for this scan geometry if accurately calibrated. These observations are also reflected quantitatively in Figure 7(c), where the ESF width (σ) is plotted versus distance from the central axial plane. The results illustrate successful application of the wire-based calibration method for a non-circular orbit known to have beneficial image quality characteristics.

Experiment #2: Comparison with BB-based Calibration in a Real Circular Scan Orbit: Figure 8 summarizes the results of Experiment #2, demonstrating ray deviation (Figure 8(a)) with a median value of 0.07 mm for the BB-based calibration and 0.05 mm for the wire-based calibration. The latter exhibits a distribution in ray deviation that was significantly lower ($p \ll 0.001$) than for BB calibration, particularly in the tails of the distribution for which the BB calibration exhibited outlier ray deviations up to 0.35 mm. The difference between the two methods – while statistically significant – is too small to have a major impact on the quality of CT image reconstruction. Such is evident in the visualization of fine details in images of the temporal bone in Figure 8(c–d), which are visually indistinguishable. Once again, we note that wire-based calibration showed uniformly low triangulation error, in spite of the possibility of degenerate vanishing points.

Wire-based calibration also demonstrated a slight improvement ($p \ll 0.001$) in the PSF width as evident in Figure 8 (b). Overall, the results demonstrate the applicability of the wire-based calibration method in real data, showing imaging performance equivalent to that with conventional BB-based calibration.

Experiment #3: Application to a Three-Arc Orbit on a Mobile C-arm: Figure 9 shows the results of Experiment #3 involving a head phantom imaged with a mobile C-arm using circular and non-circular orbits. The results largely mirror those of Experiment #1B. As expected, the non-circular (three-arc) orbit exhibits superior sampling characteristics compared to a circular orbit, evident in improved resolution of disk edges in the z-direction. Each case exhibits streak artifacts that were not observed in Experiment #1B, associated with non-geometric effects such as beam hardening. As shown in Figure 9(c), the non-circular orbit better maintains ESF width (σ) as a function of distance (z) from the central axial plane. The results demonstrate the wire calibration method in real data and validate its utility in application to non-circular orbits of a form that are becoming increasingly prevalent with advanced C-arm systems to improve image quality and expand FOV.

4 CONCLUSIONS AND DISCUSSION

This work has presented a new geometric calibration method to support cone-beam CT systems having multiple, diverse orbit geometries. The method is generally applicable to a range of orbit shapes and overcomes a variety of limitations associated with phantoms (viz., arrangements of BB markers) that have been developed with traditional, circular orbits in mind. Successful application of the method to non-circular scans was demonstrated both in simulation (a sinusoid-on-sphere orbit) and with real projection data (a 3-arc orbit) using a

prototype mobile C-arm. In both cases, cone-beam CT images exhibited the expected improvements in edge recovery when calibrated with the wire-based method.

Quantitative tests of the wire-based method also showed high calibration accuracy, as measured by forward and backprojection error metrics, for a wide range of gantry positions. Triangulation error on the order of microns and ray deviations uniformly less than 0.2 mm were observed for three simulated test orbits with typical fiducial detection noise, as well as in real circular scans. Similarly, magnification-corrected reprojection errors smaller than typical voxel sizes, and with mean/median values less than 0.1 mm, were observed in a comprehensive sweep of simulated C-arm gantry angulations. Finally, the method demonstrated high accuracy in quantifying source-detector pose parameters, even exceeding performance reported in some prior work on BB-based calibration.

In comparisons with BB-based methods, visual quality assessments showed close agreement between wire-calibrated and BB-calibrated circular scans. Trabecular temporal bone detail in a head phantom was indistinguishable visually under both methods. Quantitatively, there was also comparable performance between the two methods, with wire-based calibration even showing slight improvements ($p \ll 0.001$) with respect to both ray deviation and PSF width.

The relative performance of BB-based and wire-based calibration is a subject that merits further study. The improved performance of the wire-based methods in this work is due in part to the larger projection footprint of wires versus BBs - i.e., there are more pixel measurements underlying the line fitting than the BB centroid calculation. Undoubtedly, however, differences in conditioning of the estimation cost functions minimized in each method also played a role. The conditioning is non-trivial to analyze, as it depends on phantom geometry in both the BB and wire methods. As a first order assessment, it may be instructive to compare the condition numbers of the linear equation (3), describing line fiducials, to the analogous system (7) for BB calibration for a range of phantom designs.

While the current work demonstrates feasibility of a particular phantom design, further optimization of the wire phantom arrangement and geometry is also a ripe topic for future work. We have shown that the current phantom design robustly accomodates gantry movements on a sphere up to about 40° from the equator, a range consistent with typical C-arm workflow constraints. Motion involving large *translations* of the gantry, however, is not necessarily within the scope of the current design, since whole wire projections and/or the 3 cm separation gap (Figure 3(a)) could fall outside the visible region of the detector for sufficiently large translations. Extending the technique to such scan geometries could involve using longer wires without a separation gap, in which case parallel wire pairs are inadvisable (i.e., subject to projection overlap). While the feasibility of a line fiducial phantom without parallel wires needs further mathematical examination, the current work has demonstrated that parallel wires (and the vanishing point theory that motivates them) may not be critical to ensuring a well-posed geometry estimation. In particular, the current wire phantom design was able to accurately estimate system geometry even in views for which the parallel wire directions had degenerate vanishing points. Future work will therefore focus on experimentation with alternative wire configurations and development of

further mathematical insight on design requirements for alternative C-arm systems and scan orbits.

Acknowledgments

This work was supported by NIH grant R01-EB-017226 and academic-industry collaboration with Siemens XP.

References

Berger M, Müller K, Aichert A, Unberath M, Thies J, Choi J-H, Fahrig R, Maier A. Marker-free motion correction in weight-bearing cone-beam CT of the knee joint. Med Phys. 2016; 43:1235–48. [PubMed: 26936708]

Bian J, Yang K, Boone JM, Han X, Sidky EY, Pan X. Investigation of iterative image reconstruction in low-dose breast CT. Phys Med Biol. 2014; 59:2659–85. [PubMed: 24786683]

Boone JM, Nelson TR, Lindfors KK, Seibert JA. Dedicated Breast CT: Radiation Dose and Image Quality Evaluation. Radiology. 2001; 221:657–67. [PubMed: 11719660]

Buchanan T. The twisted cubic and camera calibration. Comput Vis Graph Image Process. 1988; 42:130–2.

Caprile B, Torre V. Using vanishing points for camera calibration. Int J Comput Vis. 1990; 4:127–39.

Carrino JA, Al Muhit A, Zbijewski W, Thawait GK, Stayman JW, Packard N, Senn R, Yang D, Foos DH, Yorkston J, Siewerdsen JH. Dedicated Cone-Beam CT System for Extremity Imaging. Radiology. 2014; 270:816–24. [PubMed: 24475803]

Cho Y, Moseley DJ, Siewerdsen JH, Jaffray DA. Accurate technique for complete geometric calibration of cone-beam computed tomography systems. Med Phys. 2005; 32:968–83. [PubMed: 15895580]

Cipolla R, Drummond T, Robertson D. Camera calibration from vanishing points in images of architectural scenes. Rev Lit Arts Am. 1999; 2:382–91.

Erdoğan H, Fessler JA. Ordered subsets algorithms for transmission tomography. Phys Med Biol. 1999; 44:2835–51. [PubMed: 10588288]

Feldkamp LA, Davis LC, Kress JW. Practical cone-beam algorithm. J Opt Soc Am A. 1984; 1:612.

Fischler, Ma, Bolles, RC. Random Sample Consensus: A Paradigm for Model Fitting with Apphcations to Image Analysis and Automated Cartography. Commun ACM. 1981; 24:381–95.

Hartley R, Zisserman A. Multiple View Geometry in Computer Vision. 2003; 2

Hu Z, Gui J, Zou J, Rong J, Zhang Q, Zheng H, Xia D. Geometric calibration of a micro-CT system and performance for insect imaging. IEEE Trans Inf Technol Biomed. 2011; 15:655–60. [PubMed: 21659036]

Jaffray DA, Siewerdsen JH, Wong JW, Martinez AA. Flat-panel cone-beam computed tomography for image-guided radiation therapy. Int J Radiat Oncol Biol Phys. 2002; 53:1337–49. [PubMed: 12128137]

Katsevich A. Image reconstruction for the circle-and-arc trajectory. Phys Med Biol. 2005; 50:2249–65. [PubMed: 15876665]

Katsevich A. Image reconstruction for the circle and line trajectory. Phys Med Biol. 2004; 49:5059–72. [PubMed: 15609558]

Kim D, Ramani S, Fessler JA. Combining ordered subsets and momentum for accelerated X-ray CT image reconstruction. IEEE Trans Med Imaging. 2015; 34:167–78. [PubMed: 25163058]

Kyriakou Y, Lapp RM, Hillebrand L, Ertel D, Kalender Wa. Simultaneous misalignment correction for approximate circular cone-beam computed tomography. Phys Med Biol. 2008; 53:6267–89. [PubMed: 18936522]

Li X, Da Z, Liu B. A generic geometric calibration method for tomographic imaging systems with flat-panel detectors--a detailed implementation guide. Med Phys. 2010; 37:3844–54. [PubMed: 20831092]

Liebowitz D, Zisserman A. Combining scene and auto-calibration constraints. Proceedings of the Seventh IEEE International Conference on Computer Vision. 1999; 1:293–300.

Mennessier C, Clackdoyle R, Noo F. Direct determination of geometric alignment parameters for cone-beam scanners. Phys Med Biol. 2009; 54:1633–60. [PubMed: 19242049]

Noo F, Clack R, White TA, Roney TJ. The dual-ellipse cross vertex path for exact reconstruction of long objects in cone-beam tomography. Phys Med Biol. 1998; 43:797–810. [PubMed: 9572505]

Noo F, Clackdoyle R, Mennessier C, White Ta, Roney TJ. Analytic method based on identification of ellipse parameters for scanner calibration in cone-beam tomography. Phys Med Biol. 2000; 45:3489–508. [PubMed: 11098919]

Ouadah, S., Jacobson, M., Stayman, J., Ehtiati, T., Weiss, C., JHS. Task-Driven Orbit Design and Implementation on a Robotic C-Arm System for Cone-Beam CT. Proc. SPIE 10132 (Medical Imaging 2017: Physics of Medical Imaging, 101320H); 2017.

Ouadah S, Stayman JW, Gang GJ, Ehtiati T, Siewerdsen JH. Self-calibration of cone-beam CT geometry using 3D-2D image registration. Phys Med Biol. 2016; 61:2613–32. [PubMed: 26961687]

Panetta D, Belcari N, Del Guerra A, Moehrs S. An optimization-based method for geometrical calibration in cone beam CT without dedicated phantoms. Phys Med Biol. 2008:53.

Patel V, Chityala RN, Hoffmann KR, Ionita CN, Bednarek DR, Rudin S. Self-calibration of a cone-beam micro-CT system. Med Phys. 2009; 36:48–58. [PubMed: 19235373]

Pauwels R. Cone beam CT for dental and maxillofacial imaging: Dose matters. Radiat Prot Dosimetry. 2015; 165:156–61. [PubMed: 25805884]

Ritschl L, Kuntz J, Fleischmann C, Kachelrieß M. The rotate-plus-shift C-arm trajectory. Part I. Complete data with less than 180° rotation. Med Phys. 2016; 43:2295–302. [PubMed: 27147341]

Rougee A, Picard CL, Trousset YL, Ponchut C. Geometrical calibration for 3D x-ray imaging. Proc SPIE. 1993; 1897:161–9.

Slagowski JM, Dunkerley DAP, Hatt CR, Speidel MA. Single-view geometric calibration for C-arm inverse geometry CT. J Med Imaging. 2017; 4:13506.

von Smekal L, Kachelriess M, Stepina E, Kalender Wa. Geometric misalignment and calibration in cone-beam tomography. Med Phys. 2004; 31:3242–66. [PubMed: 15651608]

Stayman JW, Gang GJ, Siewerdsen JH. Task-Based Optimization of Source-Detector Orbits in Interventional Cone-Beam CT. Proceedings of the International Meeting on Fully Three-Dimensional Image Reconstruction in Radiology and Nuclear Medicine. 2015

Wicklein J, Kunze H, Kalender Wa, Kyriakou Y. Image features for misalignment correction in medical flat-detector CT. Med Phys. 2012; 39:4918. [PubMed: 22894418]

Xia D, Cho S, Pan X. Reduced Circular Sinusoidal Cone-beam CT for Industrial Applications. J Xray Sci Technol. 2009:17. [PubMed: 19644211]

Xu Y, Yang S, Ma J, Li B, Wu S, Qi H, Zhou L. Simultaneous calibration phantom commission and geometry calibration in cone beam CT. Phys Med Biol. 2017; 62:N375–90. [PubMed: 28791961]

Yang K, Kwan ALC, Miller DF, Boone JM. A geometric calibration method for cone beam CT systems. Med Phys. 2006; 33:1695–706. [PubMed: 16872077]

APPENDIX

In conventional point marker based calibration, for example those based on algebraic solution of (7), it is standard (Hartley and Zisserman 2003, p. 180) to pre-normalize the 3D marker coordinates $\boldsymbol{X}$ as well as the corresponding 2D projections $\boldsymbol{x}$. Solutions can exhibit numerical conditioning problems without this step. Here, we describe an adaptation of such procedures to line marker based calibration that has proved effective in our experiments. Given input data X_i, D_i, $\boldsymbol{x}_{ij}$ to the wire-based calibration, the 3D line parameter data is normalized according to,

$$\tilde{X}_i = \frac{X_i - \sum_{i=1}^{N} X_i/N}{\sqrt{\sum_{j=1}^{N} \| X_i - \sum_{i=1}^{N} X_i/N \|^2 / 3N}}, \qquad \tilde{D}_i = \frac{D_i}{\| D_i \|}$$

The first normalization mimics a common choice in point marker based calibration, shifting the centroid of the X_i to the 3D origin and their RMS distance from the origin to $\sqrt{3}$. As a combination of shifts and scalings, it can be represented in homogeneous coordinates as $T\mathbf{X}_i$ where T is a 4×4 affine transformation matrix. To normalize the wire image sample coordinates $\mathbf{x}_{ij}$, a 3×3 affine transformation is applied,

$$U = \begin{bmatrix} d & 0 & 0 \\ 0 & d & 0 \\ 0 & 0 & 1 \end{bmatrix}^{-1}$$

where d is the average distance of the imaged lines from the origin (as determined from 2D line fits) in a given projection view. Once the calibration has been performed, resulting in a normalized 3×4 projection matrix $\hat{P}$, an un-normalized solution in the original coordinate system can be obtained as $P = U^{-1}\hat{P}T$.

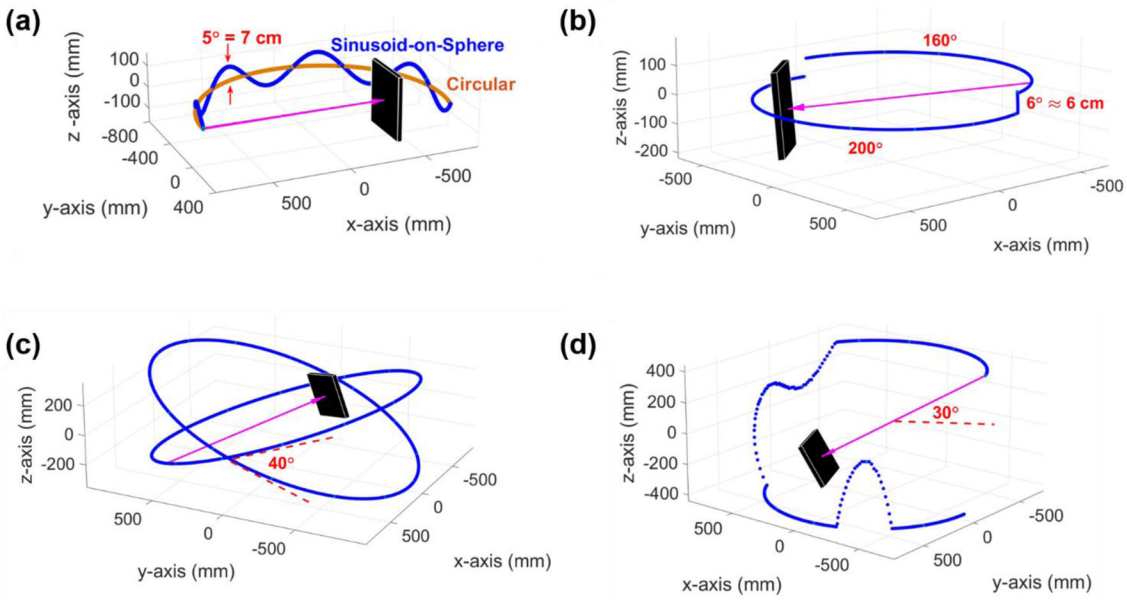

Figure 1.

Source trajectories corresponding to various scan geometries. (a) Sinusoid-on-sphere and circular trajectories. (b) A 3-arc trajectory as considered in Section 3. (c) A dual-ellipse, cross-vertex trajectory (Noo *et al* 1998). (d) A task-driven trajectory optimized to the task of visualizing a cochlear implant (Ouadah *et al* 2017).

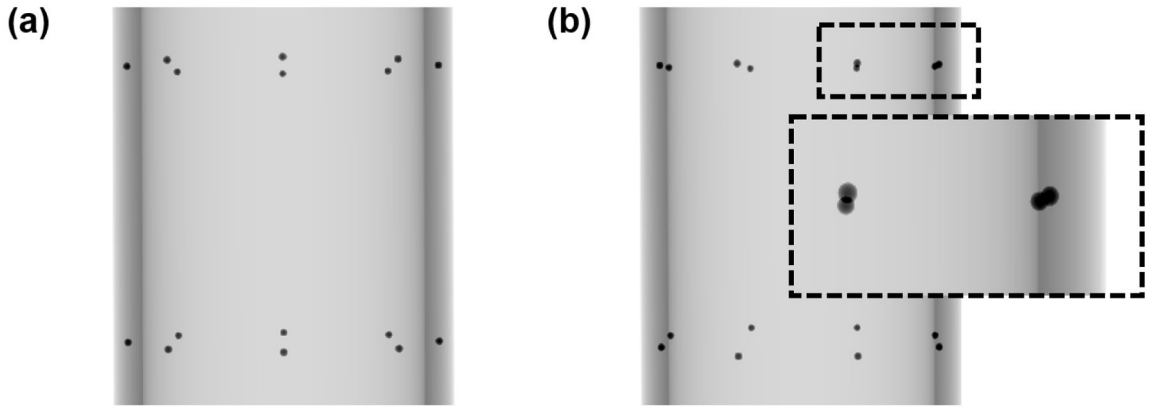

Figure 2.

Simulated projection views of a 2-ring BB phantom from (a) a conventional circular orbit and (b) a sinusoid-on-sphere orbit with oscillation amplitude 5°. For both orbits, the source trajectory radius was 78.5 cm and the Source-Detector Distance (SDD) was 120 cm. The phantom diameter was 10 cm and the axial ring separation was 9 cm.

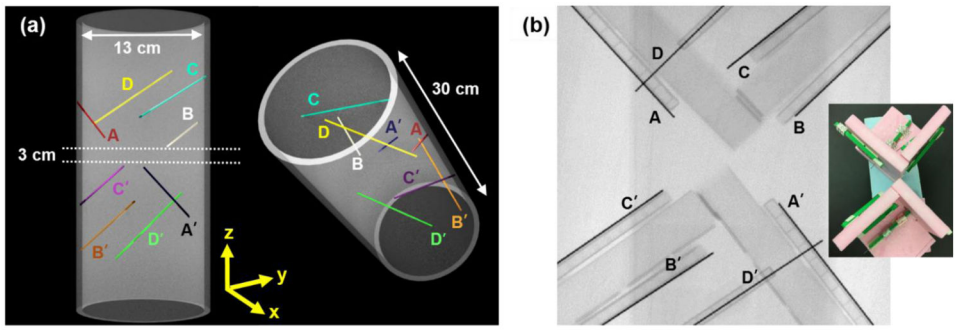

Figure 3.
Wire calibration phantom. (a) CAD rendering of a nominal 8-wire phantom design. (b) Photo and projection view of the 8-wire phantom experimental prototype.

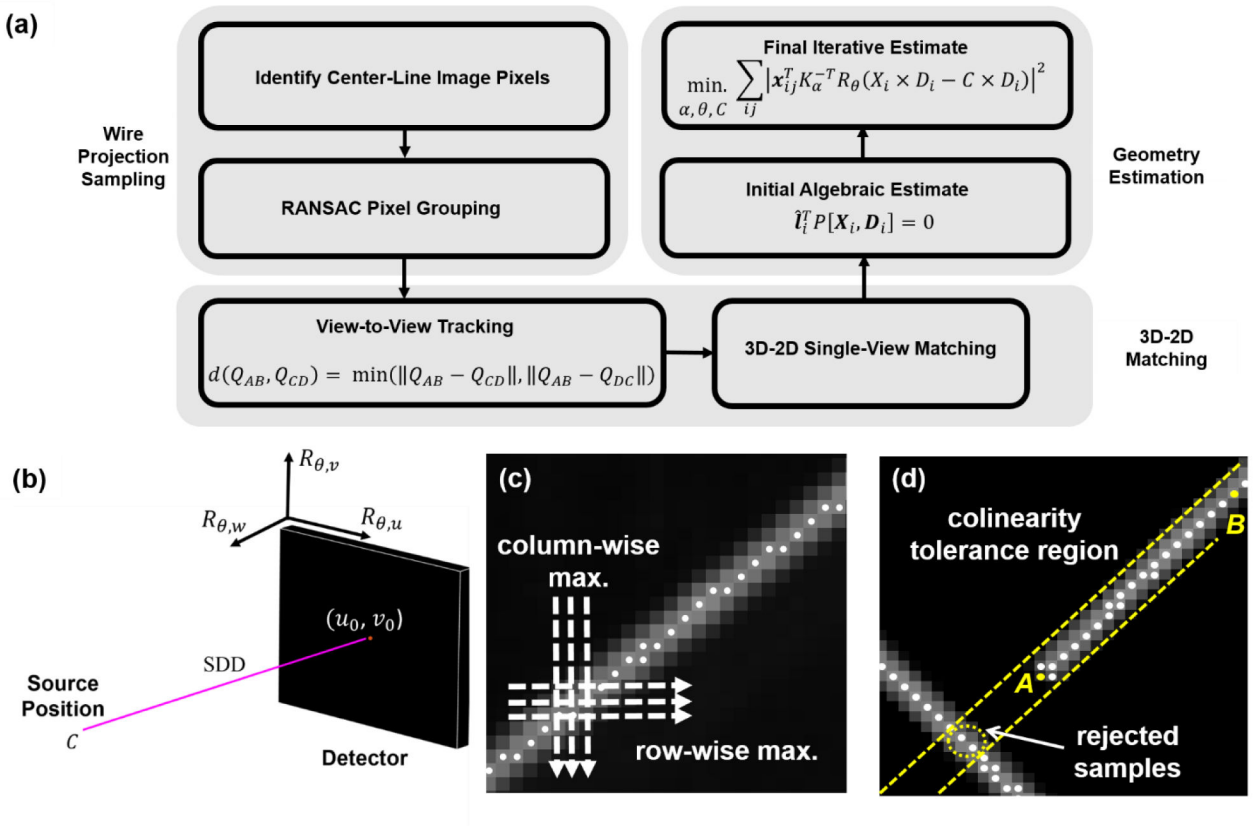

Figure 4.

(a) Flowchart of wire-based calibration method. (b) Parameterization of 9-DOF projection view geometry. (c) Sampling of wire segment projections. (d) RANSAC-based grouping of wire image samples.

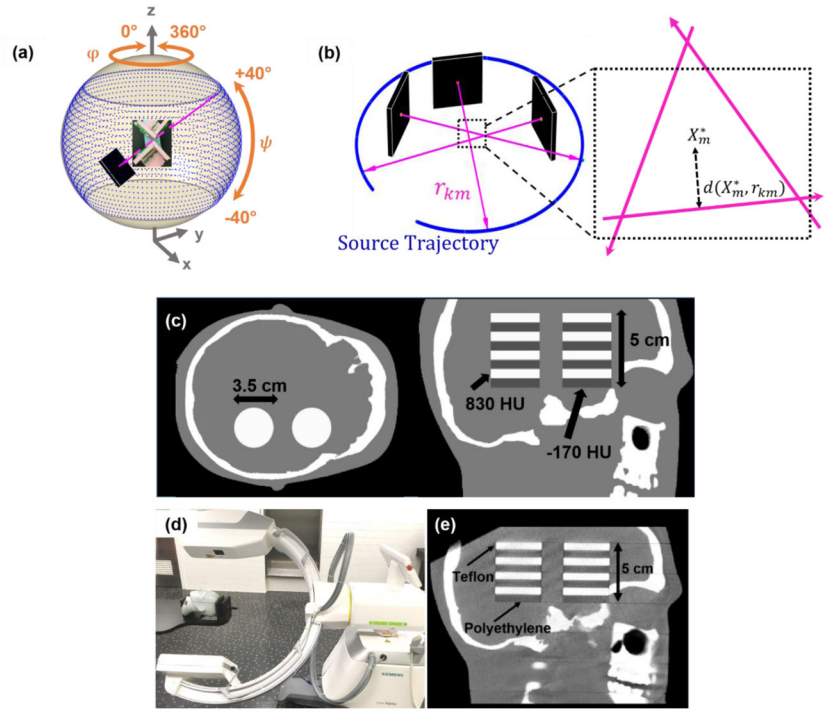

Figure 5.

Experimental methods. (a) Sampling of gantry poses in spherical coordinates used in calibration accuracy simulation tests. (b) Illustration of triangulation ray deviation metric. (c) A digital head phantom with 2 stacks of high contrast disks. (d) Prototype mobile C-arm for cone-beam CT based on the Cios Alpha (Siemens Healthineers). (e) Real head phantom with 2 stacks of polyethylene and Teflon disks.

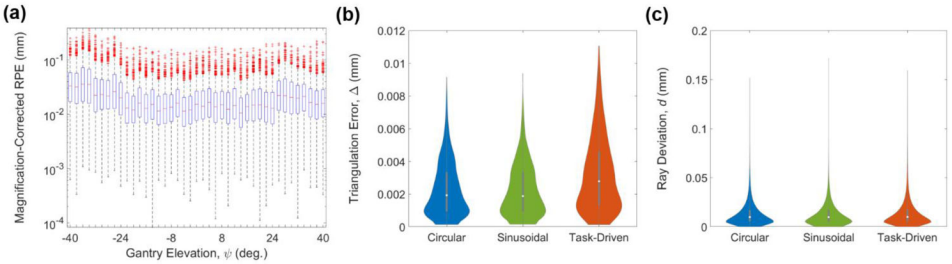

Figure 6. Experiment #1A: Simulation Tests of Geometry Estimation Accuracy

Distributions of various forward and back projection errors. All are based on 50 independent noise realizations. (a) Box plot of magnification-corrected RPE at various out-of-plane gantry elevations, ψ, computed from samples over both noise realizations and test points. At each elevation, worst-case distributions are shown, meaning the distribution for the azimuthal position with the largest outliers. (b) Violin plots of triangulation error, Δ, computed from samples over all noise realizations, test points, and views. Median and interquartile range are also shown in each case. (b) The same for ray deviation, *d*.

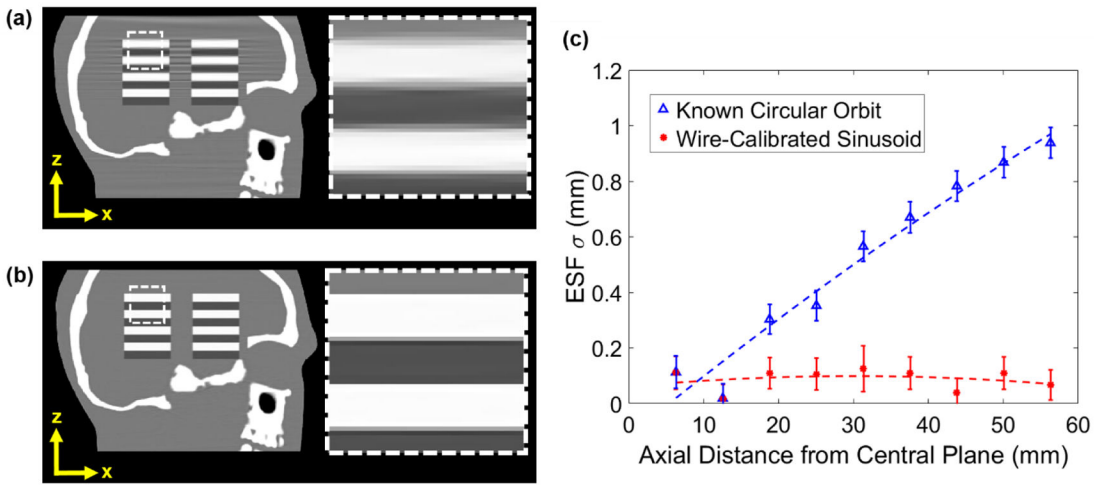

Figure 7. Experiment #1B: Simulated Integration into a CBCT Imaging Chain

Images of the digital head phantom reconstructed using the PWLS algorithm for (a) a known circular scan geometry and (b) a sinusoid-on-sphere geometry calibrated with the wire-based calibration method. (c) Plot of ESF width σ as a function of distance from the central axial plane.

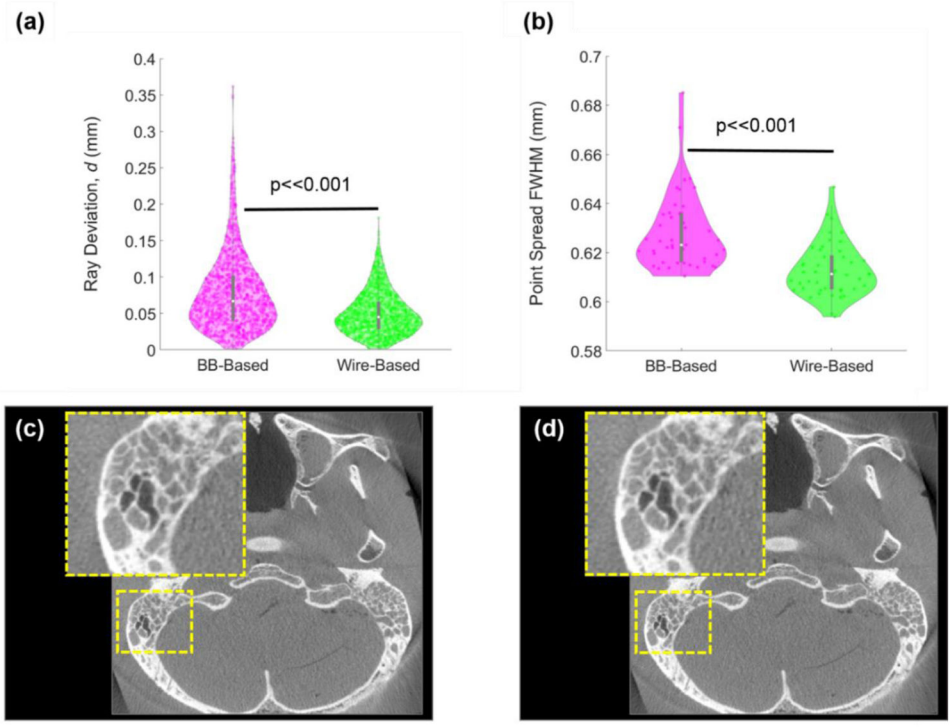

Figure 8. Experiment #2: Comparison with BB-based Calibration in a Real Circular Scan Orbit

(a) Distribution of ray deviation for BB and wire calibration methods as measured with a 4-marker phantom. The ensembles range over gantry positions and markers. (b) Distributions of the FWHM in PSF for the two calibration methods. The images show FDK reconstructions of a head phantom for (c) BB-based calibration and (d) wire-based calibration.

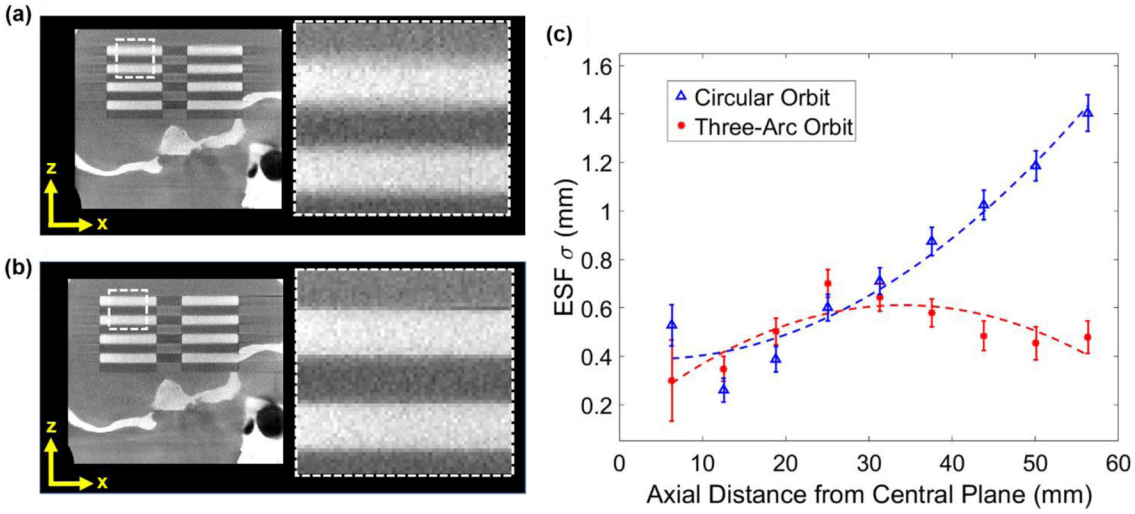

Figure 9. Experiment #3: Application to a Three-Arc Orbit on a Mobile C-arm

(a) Sagittal images of a head phantom (reconstructed using the PPL algorithm) containing stacks of disks, scanned using a circular trajectory with geometric calibration by the BB method. (b) The same, scanned using the three-arc orbit of Figure 1(b) with geometric calibration by the wire method. (c) Plot of ESF width σ as a function of distance from the central axial plane.

Table 1

Wire pose data for nominal phantom design and the estimated poses for the prototype phantom implementation.

		A	B	C	D	A′	B′	C′	D′
Nominal Design	X_x (mm)	56.10	2.08	78.08	−6.73	8.66	78.08	2.08	−6.73
	X_y (mm)	−3.79	46.08	22.08	−23.63	24.16	−1.71	−25.71	44.00
	X_z (mm)	7.73	3.34	31.13	20.31	−31.06	−54.46	−26.66	−43.63
	D_x (mm)	0.0442	0.7221	−0.6904	0.0224	−0.0442	−0.7221	0.6904	−0.0224
	D_y (mm)	−0.6906	0.5215	0.5011	0.7231	0.6906	−0.5215	−0.5011	−0.7231
	D_z (mm)	0.7219	0.4546	0.5217	0.6904	−0.7219	−0.4546	−0.5217	−0.6904
Implemented Prototype	X_x (mm)	51.40	2.44	68.01	−13.34	19.28	72.20	6.22	5.40
	X_y (mm)	−12.99	42.78	10.75	−36.05	34.60	5.73	−20.00	56.65
	X_z (mm)	6.45	11.25	27.15	24.75	−32.25	−55.05	−25.65	−49.95
	D_x (mm)	0.0728	0.6846	−0.6346	0.0019	0.0080	−0.5706	0.6556	0.0248
	D_y (mm)	−0.6691	0.5350	0.5538	0.7012	0.6074	−0.6796	−0.5902	−0.8258
	D_z (mm)	0.7396	0.4951	0.5391	0.7130	−0.7944	−0.4610	−0.4709	−0.5634

Phys Med Biol. Author manuscript; available in PMC 2019 January 16.

Table 2

Errors in magnification and various source-detector pose parameters from simulated wire-based calibrations for several orbit geometries. Error mean and standard deviation are taken with respect to 50 measurements over all orbit views. Magnification was computed from 16 test points.

		Source Location (mm)			Detector Center (mm)			Detector Orientation (deg)		
		c_u	c_v	c_w	FP_u	FP_v	FP_w	$R_{\theta,w}$	Skew	Mag. (%)
Circular	Mean	0.066	0.088	1.145	0.032	0.044	0.581	0.092	0.002	0.014
	Std Dev	0.073	0.081	0.933	0.033	0.040	0.456	0.053	0.002	0.013
Sinsoidal	Mean	0.063	0.087	1.157	0.030	0.044	0.588	0.092	0.004	0.014
	Std Dev	0.066	0.077	0.943	0.030	0.038	0.462	0.053	0.004	0.013
Task-Driven	Mean	0.100	0.068	1.274	0.050	0.034	0.642	0.096	0.030	0.015
	Std Dev	0.113	0.065	1.017	0.057	0.032	0.513	0.067	0.028	0.014